Titin-Mediated Viscoelastic Passive Muscle Mechanics

Filip Ježek[1,4], Anthony J. Baker[2], David Nordsletten[3], and Daniel A. Beard[*1]

[1]Department of Molecular and Integrative Physiology, University of Michigan, Ann Arbor, MI, USA
[3]Departments of Biomedical Engineering and Cardiac Surgery, University of Michigan, Ann Arbor, MI, USA
[2]Veterans Affairs Medical Center, San Francisco, CA, and Department of Medicine, University of California, San Francisco, CA, USA
[4]Institute of Pathological Physiology, 1st Faculty of Medicine, Charles University, Prague, CZ

March 25, 2024

Abstract

This study investigates the mechanical properties of titin, a sarcomeric structural protein that links the myosin thick filament to the Z disk. The elastic region of titin, located in the I band of striated muscle sarcomeres, plays a vital role in providing the passive restoring force during muscle stretch. Under stress, serial globular domains within the elastic region of the titin molecule reversibly unfold. This unfolding phenomenon contributes to both hysteresis (a lag in stress between loading and unloading) and preconditioning effects in striated muscle mechanics. Moreover, experiments reveal that stress relaxation in titin follows a power law decay, and that titin's nonlinear stress-strain relationship and hysteresis behavior are calcium dependent. To comprehensively analyze these mechanical phenomena, we develop, analyze, and simulate a mesoscopic-scale ensemble model of titin elastic domain mechanics that accounts for the dynamic unfolding of globular domains along the titin chain. Providing a unified basis for observed viscoelastic and preconditioning effects, calcium dependency, and power-law stress relaxation phenomena, this study introduces a novel theoretical basis for understanding and simulating the role of titin in striated muscle mechanics.

Introduction

Titin is a large filamentous protein that connects the Z-disk to the myosin thick filament in sarcomeres and functions as a molecular spring, contributing to the passive mechanical properties of striated muscle, as illustrated in Figure 1. Titin also plays a key role in organizing the sarcomeric structure, ensuring the alignment of contractile proteins, and aiding in the transmission of force during muscle contraction. Single-molecule atomic force microscopy reveals that when the titin molecule is stretched, serial globular immunoglobulin-like (Ig) domains in the titin chain unfold sequentially, resulting in a non-monotonic force-extension relationship [21]. The reversible Ig domain folding behavior is thought to contribute to governing the viscoelastic and hysteresis behaviors in passive stress-strain relationships in muscle [18].

Because titin is the major sarcomeric structural element that provides a restoring force to oppose passive elongation, its mechanical properties are a fundamental determinant of myocardial diastolic function. At sarcomere lengths of roughly 2.1 μm and less, titin is estimated to contribute the majority of the total measured passive tension [6, 9, 24]. Thus the passive pressure-volume relationship associated with diastolic filling of the chambers of the heart is governed, at the cellular and molecular levels, in part by titin mechanics [6, 5, 2]. Phosphorylations of titin residues via PKA, PKD, and PKG kinases in the myocardium are associated with reductions in titin-mediated passive stiffness, while phosphorylation of PKC targets are associated with increased passive stiffness [16, 11, 17]. Thus, the passive mechanical behavior of the myocardium is physiologically regulated via various signalling pathways that regulate the molecular mechanical properties of titin.

Calcium ion concentration is also known to play an important role in regulating the mechanical properties and function of titin. Labeit et al. [15] found the stiffness of the PEVK segment of human titin is sensitive to Ca^{2+}, which alters the apparent persistence length associated with the unstressed molecule. Increasing calcium concentration lowers the persistence length or, equivalently, increases the passive elastic resistance to elongation. Kulke et al. [14] showed that the PEVK domain binds to actin in a Ca^{2+}-dependent manner. Squarci et al. [23] observed a muscle activation-dependent mechanical "rectifier" behavior, interpreted as the PEVK segment reversibly attaching to the actin fiber in the intact muscle, as illustrated in Figure 1.

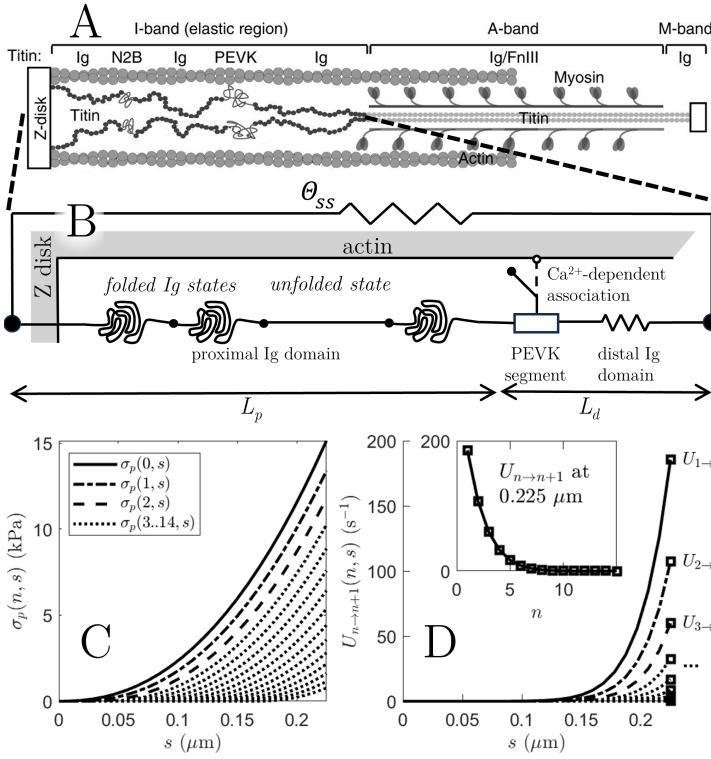*Corresponding author. Email: beardda@umich.edu

Figure 1: Illustration of titin composition in sarcomere and schematic of model. A. The incorporation of titin into the sarcomere is illustrated, with the titin elastic region in the I-band connecting the myosin thick filament to the Z-disk (adapted from [4] under CC by 4 international license https://creativecommons.org/licenses/by/4.0/). B. The diagram illustrates the model composition for the titin elastic region. The proximal domain (between the Z-disk attachment and the PEVK domain) is modeled as a series of globular Ig components that can exist in folded or unfolded states. Distal to the PEVK segment is a nonlinear spring labeled "distal Ig domain". C. The relationship between stress in the proximal domain $\sigma_p(n,s)$ and strain of the proximal domain, s, is plotted for different values of n, the number of unfolded Ig states in a chain. D. The relationship between unfolding rate $U_{n \to n+1}$ and strain of the proximal domain, s, is plotted for different values of n. Both stress and unfolding rate increase with s, and decrease with increasing n.

Titin's mechanical behavior arises from unique structural features and functional mechanisms. Its structure is characterized by repeating immunoglobulin-like (Ig) and fibronectin (Fn) domains, akin to molecular beads on a string. This modular arrangement allows for extensibility, as each Ig and Fn domain can independently unfold and refold, acting as molecular springs [13, 9, 5]. The extensibility of titin is particularly prominent in the I-band region, which is rich in these domains. Given the fundamental role of titin in determining the passive mechanical properties of muscle, and given the fact that titin mechanical function is dynamically regulated by posttranslational modifications and intracellular calcium, it is not surprising that titin mutations are linked to multiple myopathies [3], including restrictive cardiomyopathy [20], dilated cardiomyopathy[10], and muscular dystrophies [12]. Under-

standing the molecular-mechanical function of titin is crucial to understanding the mechanisms underlying these mutations.

The overall goals of this study were to quantitatively assess the dynamic and calcium-dependent properties of titin mechanics in the intact cardiac sarcomere, and to describe the behavior of the system in a self-consistent mathematical model. Baker et al. [1] assessed the Ca^{2+}-dependence of the stress response to stretch of permeabilized murine right ventricular trabeculae, showing that addition of Ca^{2+} increases the apparent viscous component of the stress response. Here, data from Baker et al. are analyzed to develop and identify our theoretical model of the viscoelastic passive mechanical response to stretch in these fibers. To characterize the passive myocardial properties, permeabilized mouse trabecular fibers were stretched over a half-sarcomere lengths from 0.95 to 1.175 μm at ramp speeds ranging from 0.00225 to 2.25 μm·sec^{-1}, and then allowed to relax for several seconds to minutes. While the rate of tension increase during the stretch phase of the experiment was, unsurprisingly, determined by the speed of the stretch, the rate of tension decay following stretch was, remarkably, observed to following a time-scale independent power-law timecourse. In the presence of calcium and para-nitroblebbistatin the peak tension increased with increasing calcium. A mathematical model, integrating unfolding of a series of globular elements and a calcium-dependent PEVK-actin binding mechanism (Figure 1), was developed to analyze data from these experiments. Integrating these mechanisms, the model is able to effectively capture the calcium- and stretch-dependent peak tension as well as the tension decay kinetics observed at different calcium levels. The power-law nature of tension decay is predicted to emerge as a property of the sequence of globular elements, each capable of unfolding and introducing a finite amount of slack into the chain. Equivalently, each unfolding event increases the persistence length of the chain. With each unfolding event, the tension sensed by unfolded elements in the chain decreases, reducing the effective rate of unfolding. As a result, the time scale of decay increases with decreasing tension during the decay process.

The model developed to simulate these processes represents a unique new tool to investigate passive myocardial mechanics and mechanistically represent titin mechanics at a mesoscopic scale. The model also represents a tool for testing and refining hypotheses on the function and regulation of passive myocardial mechanics, and as a building block for integrated modeling of myocardial cell and tissue mechanics.

Methods

Experimental Data on Passive Muscle Mechanics

Data analyzed in this paper are reported in the accompanying paper [1]. In brief, right ventricular demembranated trabeculae of 12 week old male (n=2) and female (n = 3) mice were subjected to ramp length extensions from 0.95 to 1.175 mus-

cle length (L_0), where L_0 was established by adjusting muscle length (ML) to set the sarcomere length to 2.0 μm. Muscle dimensions, and active and passive forces were measured at L_0 and at 21° C. The ramp length extension times range from $t_r = 0.1$ s to 100 s, corresponding to velocities of 2.25 to 0.00225 L_0/s. Following extension, the muscle was held fixed at ML $= 1.175L_0$ for 60 seconds. Muscle stress response to this strain protocol was observed in Ca^{2+}-free relaxing solution (denoted pCa$= 11$), at saturating calcium conditions (pCa$= 4.51$) to measure maximal stress, and in solution with para-nitro-blebbistatin (PNB), deactivating the cross-bridge force generation. The strain protocol was repeated with PNB present at five different calcium concentrations: pCa $= 4.51$, 5.5, 5.75, 6 and 6.25.
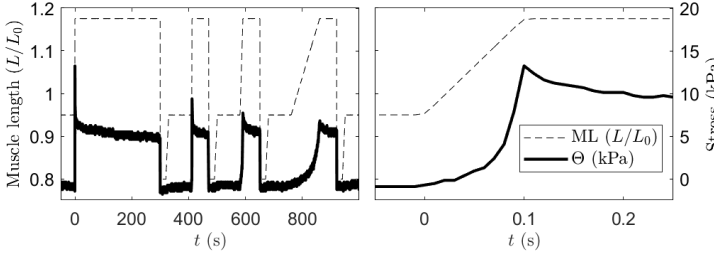

Figure 2: Representative set of measured muscle stress during ramp-up and decay. During the ramp increases in length, muscle length (ML) was extended from $0.95L_0$ to $1.175L_0$ for ramp times of 0.1, 1, 10, and 100 seconds. The right panel shows a detail of muscle length and stress Θ as functions of time for the fastest ramp (0.1 second). Stress increases in a concave-up manner during the ramp increase in length, achieves a peak value at the end of the ramp increase, and then decays.

An example time course of stress measured at pCa$= 11$ during this protocol is illustrated in Figure 2, showing that the peak stress is highest for the most rapid ramp speed. Peak stress is approximately 15 kPa for the fastest ramp, and approximately 6 kPa for the slowest ramp. Regardless of peak stress, the stress relaxes to approximately 5 kPa following the ramp.

Procedures for correcting for transducer drift and other artefacts in the data and averaging data from multiple experiments are detailed in the Appendix.

Computational Model

The mathematical model of I-band mechanics takes the form of an ensemble of titin chains, with a single member of the ensemble illustrated schematically in Figure 1. The structure of the model is similar to that of Heidlauf et al. [8, 7]. The single titin chain comprises proximal and distal Ig domains and a proline-, glutamic acid-, valine, and lysine-enriched domain, or PEVK segment, connected in series. The total length of the protein is denoted $L = L_p + L_d$, with L_p and L_d denoting length in the proximal and distal segments. Strain in the proximal domain denoted s, which is defined in reference to a reference muscle length L_0:

$$s = L_p - 0.95L_0$$

where $L_0 = 1$ μm is a reference half-sarcomere length, and $0.95L_0$ is the initial half-sarcomere length in the ramp extension experiments used to identify the model. The model explicitly tracks the ensemble distribution of strain s and number of unfolded domains n in the proximal chain. (As a simplifying assumption unfolding events are treated only in the proximal chain.) The titin strand is assumed to attach to and detach from a neighboring actin filament at the PEVK site, located between the proximal and distal Ig chain domains. The actin-bound configuration is referred to as the attached state. The unbound configuration is referred to as the unattached state.

Table 1: Variables in Model

Variable	Description	Units
Independent variables		
t	time	seconds
s	strain in proximal chain	μm
n	number of unfolded globules in proximal chain	discrete, unitless
Dependent variables		
$p_u(n,s,t)$	probability density for (n,s) in unattached chains	μm^{-1}
$p_a(n,s,t)$	probability density for (n,s) in attached chains	μm^{-1}
$\sigma_p(n,s)$	stress in proximal titin chain	kPa
$\sigma_d(n,s)$	stress in distal titin chain	kPa
$\Theta_p(n,s)$	average stress in ensemble of proximal titin chains	kPa
$\Theta_d(n,s)$	average stress in ensemble of distal titin chains	kPa
$\Theta(t)$	total stress in muscle fiber	kPa
$L(t)$	length of 1/2 sarcomere	μm

The variables in the model are listed and summarized in Table 1. The total stress of the muscle arises from contributions from unattached states, attached states, and contributions from parallel non-titin components. The function $p_u(n,s,t)$ is the ensemble probability density of n, number of unfolded states per chain, and s, stretch, in unattached chains, such that

$$\sum_{n=0}^{N} \int_0^\infty p_u(n,s,t)ds$$

represents the fraction of titin chains that are in the unattached state. Similarly the function $p_a(n,s,t)$ is the ensemble probability density of n, number of unfolded states per chain, and s, stretch, in attached chains, such that

$$\sum_{n=0}^{N} \int_0^\infty p_a(n,s,t)ds$$

represents the fraction of chains in the attached state. These fractions obey

$$1 = \sum_{n=0}^{N} \int_0^\infty p_u(n,s,t)ds + \sum_{n=0}^{N} \int_0^\infty p_a(n,s,t)ds. \quad (1)$$

3

Table 2: Adjustable parameters in model

Parameter	Description	Value	Units
adjustable parameters			
k_p	proportionality constant for proximal chain length-stress relation (pCa = 11)	467.6	kPa
k_p	proportionality constant for proximal chain length-stress relation (pCa = 4.51)	1732.9	kPa
k_d	proportionality constant for distal chain length-stress relation (pCa = 11)	38.3×10^3	kPa
k_d	proportionality constant for distal chain length-stress relation (pCa = 4.51)	50.4×10^3	kPa
α_U	proportionality constant for unfolding rate	8.36×10^6	sec^{-1}
k_A	rate of attachment of PEVK element to actin (pCa = 11)	0	sec^{-1}
k_A	rate of attachment of PEVK element to actin (pCa = 4.51)	4.98	sec^{-1}
k_D	rate of detachment of PEVK element from actin	84.9	sec^{-1}
n_p	exponent for proximal chain length-stress relation	2.30	unitless
n_d	exponent for distal chain length-stress relation	2.33	unitless
n_U	exponent for unfolding rate	9.0	unitless
Δ_U	slack length associated with unfolding one Ig unit	0.0117	μm
k_{ss}	proportionality constant of the parallel spring	958×10^6	kPa
n_{ss}	exponent for the parallel spring	12.8	unitless
fixed parameters			
N_g	number of Ig units in chain	15	unitless
L_0	reference half-sarcomere length	1.0	μm
μ	viscosity of dashpot element	0.1	kPa·sec·μm^{-1}

The stress in an individual proximal titin chain domain is assumed proportional to stretch s

$$\sigma_p(n, s) = k_p \cdot \max\left(0, (s - n\Delta_U)/L_0\right)^{n_p}, \quad n = 0, 1, \ldots N \quad (2)$$

where Δ_U is the slack length associated with the unfolding of one proximal Ig domain element, L_0 is a reference half-sarcomere length taken to be 1.0 μm, and N_g is the total number of Ig domains assumed in the chain. The relationship between $\sigma_p(n, s)$ and s is illustrated in Figure 1C. The average stress associated with the ensemble of unattached titin chains is computed

$$\Theta_u(t) = \sum_{n=0}^{N} \int_0^\infty \sigma_p(n, s) p_u(n, s, t) ds. \quad (3)$$

The distal Ig domain is assumed to behave like a nonlinear spring. The stress in this element is assumed proportional to stretch of the element $L - s - 0.95L_0$:

$$\sigma_d(n, s) = k_d \cdot \max\left(0, (L - s - 0.95L_0)/L_0\right)^{n_d}. \quad (4)$$

The average stress associated with the ensemble of distal domains is computed

$$\Theta_d(t) = \sum_{n=0}^{N} \int_0^\infty \sigma_d(n, s) \left(p_a(n, s, t) + p_u(n, s, t)\right) ds. \quad (5)$$

Here titin molecules in both the unattached and attached states contribute to the total force.

Proximal and distal forces in an individual chain are assumed to be balanced, $\sigma_d(n, s) = \sigma_p(n, s)$. This force balance is achieved in the model by deforming the proximal chain with velocity

$$v_p(n, s) = \left(\sigma_d(n, s) - \sigma_p(n, s)\right)/\mu, \quad (6)$$

where μ is a viscosity factor that is treated as an arbitrary parameter with value set low enough to achieve an effective force balance throughout the simulations. Thus μ is does not represent a physical viscosity and its value is set such that model behavior is not sensitive to it.

Unfolding of a single Ig domain, associated with a chain transition from state n to $n + 1$, occurs at a rate that is proportional to the strain on the globular chain:

$$U_{n \to n+1}(n, s) = \alpha_U \left(\frac{s - n\Delta_U}{L_0}\right)^{n_U} \quad (7)$$

where Δ_U is the slack associated with one globule unfolding. The unfolding rate $U_{n \to n+1}(n, s)$ is plotted as a function of s in Figure 1D. Refolding events—transitions from state n to $n - 1$—are not considered in the current model.

With the rates of stretching and unfolding defined by Equations (6) and (7), the governing equation for $p_u(n, s)$—the probability density of n and s for unattached chain states—is

$$
\begin{aligned}
\frac{\partial p_u(0, s)}{\partial t} = \ & -v_p(0, s)\frac{\partial p_u(0, s)}{\partial s} \\
& -U_{0 \to 1}(0, s) N_g p_u(0, s) \\
& -k_A p_u(0, s) + k_D p_a(0, s) \\
\frac{\partial p_u(n, s)}{\partial t} = \ & -v_p(n, s)\frac{\partial p_u(n, s)}{\partial s} \\
& -U_{n \to n+1}(n, s)\left(N_g - n\right) p_u(n, s) \\
& +U_{n-1 \to n}(n-1, s)\left(N_g - n + 1\right) p_u(n-1, s) \\
& -k_A p_u(n, s) + k_D p_a(n, s), \quad n = 1 \ldots N. \quad (8)
\end{aligned}
$$

Similarly, the governing equation for $p_a(n, s)$—the probability

4

density of n and s for attached chain states—is

$$\frac{\partial p_a(0,s)}{\partial t} = -U_{0\to1}(0,s)p_a(0,s)$$
$$+k_A p_u(0,s) - k_D N_g p_a(0,s)$$

$$\frac{\partial p_a(n,s)}{\partial t} = -U_{n\to n+1}(n,s)\left(N_g - n\right)p_a(n,s)$$
$$+U_{n-1\to n}(n-1,s)\left(N_g - n + 1\right)p_a(n-1,s)$$
$$+k_A p_u(n,s) - k_D p_a(n,s), \ n = 1\ldots N. \quad (9)$$

Equations (8) and (9) assume that attachment and detachment of the PEVK domain of the titin chain to actin occur at rates k_A and k_D. For calcium-free conditions (pCa = 11) $k_A = 0$ and no attachment occurs.

Model parameter definitions and estimated values are listed in Table 2. The force proportionality constants k_p and k_d and the PEVK attachment rate k_A are assumed to be calcium-dependent. The value of N_g is set to 15, a value that ensures that the strain in the proximal chain for the half-sarcomere extension in the experiments analyzed remains less than $N_g\Delta_U$. Thus N_g is not meant to represent the true number of Ig domains in the proximal chain. Rather N_g and Δ_U reflect the numerical discretization of the system.

The total passive muscle stress is computed from a sum of contributions from titin and from a parallel nonlinear spring that represents the steady state stress at a given length:

$$\Theta(t) = \Theta_d(t) + k_{ss}\left(\frac{L - 0.95L_0}{L_0}\right)^{n_{ss}} \quad (10)$$

For the ramp extension experiments simulated here the initial state of the model is $p_u(n,s) = \delta(s)\delta_{0,n}$ and $p_a(n,s) = 0$, assuming no attachment to actin with zero strain and all globular elements in the folded state. Prior to initiating the ramp-up, the model is run to reach an initial steady-state. Computer codes for simulating the model are available at `https://github.com/beards-lab/TitinViscoelasticity`.

Results

Properties of the stress relaxation

Average stress time-course data from experiments of Baker et al. [1] at pCa = 11 are plotted in Figure 3 on linear, semilog-y, and log-log scales. To plot the data on semilog-y and log-log scales a common long-time steady-state stress level Θ_∞ was estimated and the data were shifted in time so that the decaying tails of the stress data were optimally overlaying. For these data the estimated value of Θ_∞ is 4.90 kPa, and the total stress minus the steady-state stress, $\Theta - \Theta_\infty$ is plotted on the y-axes in the semilog and log-log panels in Figure 3. The time shifts used to overlay the decay tails are indicated in the figure.

Figure 3 illustrates that the stress decay process does not follow exponential kinetics (does not follow a straight line on the semilog-y plot). Rather, the decay follows a power-law with $\Theta \sim t^{-0.21}$. This power-law decay is independent of the
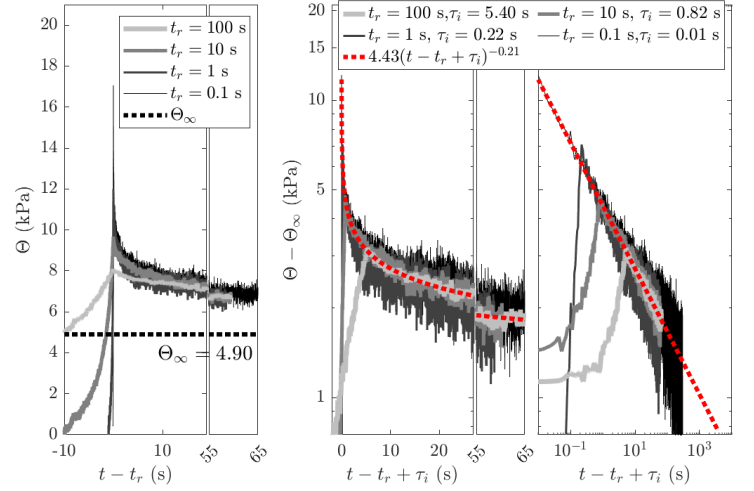

Figure 3: Analysis of stress decay in muscle fibers. The left panel plots stress versus time for the four ramp speeds on a linear scale. The middle and right panels plot stress versus time for the four ramp speeds on semilog-y and log-log scales. The semilog and log-log plots show a power-law function fit to the tail of the decay curves for all ramps. The ramp times $t_r = 0.1$ s to 100 s and time shifts τ_i for the semilog and log-log plots are indicated in the figure inset.

ramp speed or peak height. Moreover, the observed power-law decay, with an exponent of -0.21, suggests that stress decay may extend over extraordinarily long time scales. This result also compares remarkably well with behavior observed for human myocardium, which shows a power-law decay, with an exponent of -0.184 [19]. As illustrated in the figure, the extrapolation of the power-law decay predicts a contribution of 1 kPa to the passive stress 1000 seconds after the peak stress. At this rate of decay, it would take over 5×10^7 seconds to decay to 0.1 kPa! Thus, the estimated Θ_∞ of 4.90 kPa is lower than the apparent steady-state stress observed 30 seconds after the peak stress reported by Baker et al. [1].

Model analysis of passive muscle dynamics under Ca^{2+}-free conditions

Figure 4 shows optimal model fits to stress data collected under calcium-free (pCa = 11) conditions. The ramp times t_r indicated in the figure denote the length of time each ramp takes. The greatest peak stress is associated with the fastest ramp, $t_r = 0.1$ seconds. The computational model is able to correctly match not only the peak heights for different ramp durations, but also the stress increase during ramp up and the decay time course. The right panel of Figure 4 shows that the model is also able to capture the observed power law decay in stress, with stress decay in the model following $\Theta \sim t^{-0.24}$ over three decades in time.

The probability state space of the simulated ensemble of titin elastic chains, $p_u(n,s)$, during the fastest ramp stretch and decay is illustrated in Figure 5, which shows the state probability as heat maps in the (n,s) space at different time points in the experiment. In the initial state all chains are
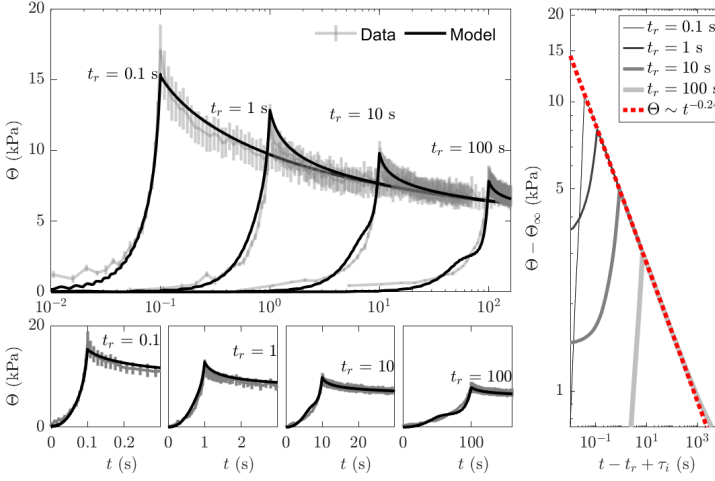
Figure 4: Model fit to stress data following ramp increases in muscle length at zero calcium (pCa = 11). A. For all time courses the muscle is lengthened from $0.95L_0$ to $1.175L_0$ in a linear ramp and then held at the final length to observe the stress decay. The top panel show stress data and optimal model fit on a semilog-x plot. The bottom panel shows the peak and initial stress decay on linear scale plots for each ramp time, from $t_r = 0.1$ seconds to $t_r = 100$ seconds. B. Model-predicted stress decay is shown on a log-log plot illustrating the power-law behavior $\Theta \sim t^{-0.24}$.

Figure 5: Probability space of simulated chain at low calcium. Top: the probability density $p_u(n,s)$ is illustrated as a heat map, with contours drawn at 1%, at four different times in the simulation of the fast ramp extension experiment for the low-calcium condition. The bottom panel shows the simulated stress time course and the four time points ($t = 10^{-3}$, 0.1, 0.2, and 1000 seconds) for which the the probability density $p_u(n,s)$ is illustrated in top panels as a per cent of all states.

unfolded, there is no strain on the titin chain, and thus $p_u(n,s) = \delta(s)\delta_{0,n}$. When chain is rapidly stretched by 0.225 μm, at time $t = 0.1$ seconds, $p_u(n,s)$ has a peak at approximately $s = 0.19$ μm and $n = 0$, meaning that the proximal part of the chain is stretched by approximately 0.19 μm and the distal part by 0.04 μm. At this time point there is also nonzero-probability at $n \geq 1$, meaning that some of the chains in the simulated ensemble have begun to unfold. During the relaxation phase of the experiment the the peak in the probability density shifts to higher values of n. At the final time point in the simulation ($t = 1000$ seconds), the peak of $p_u(n,s)$ is at $n = 13$ and $s \approx 0.22$ μm, associated with a strain in the proximal chain of 0.22 μm with 13 globular units in the titin chain unfolded. Since each unfolding introduces Δ_U slack in the chain, the final state is associated with roughy $13\Delta_U = 0.15$ μm of slack in the chain.

Model analysis of passive muscle dynamics under high-Ca^{2+} conditions

Figure 6 shows optimal model fits to stress data collected under high-calcium (pCa = 4.51) conditions. Similar to the stress response at low calcium, the greatest peak stress is associated with the fastest ramp, $t_r = 0.1$ seconds. The peak stresses at each extension speed are all markedly higher at pCa = 4.51 compared to peak stresses at pCa = 11. The model captures this Ca^{2+}-induced increase in peak force through the Ca^{2+}-dependence of chain stiffness and PEVK domain attachment to actin.

The stress decay time courses are plotted in a log-log scale in the right panel. The model predicts that stress relaxation
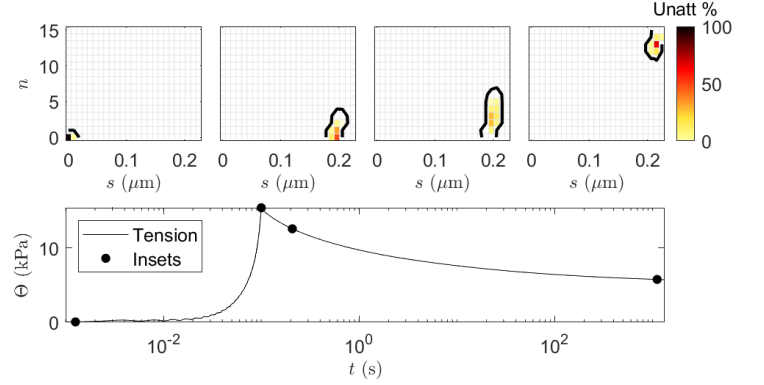
at high calcium follows essentially the same power law as observed at low calcium, with $\Theta \sim t^{-0.23}$, suggesting that the calcium does not affect the power-law nature of stress relaxation. However, the match between the model and the data for the tail component of the stress relaxation curve is determined by procedures described in the Appendix for correcting for incomplete inhibition of active tension. In brief, an active force component of the tail component of the high-calcium stress-relaxation is subtracted from the raw data using the imposed assumption that the stress relaxation time-course follows this power law. Thus, unlike the $\Theta \sim t^{-0.24}$ behavior shown in Figure 4, the $\Theta \sim t^{-0.23}$ behavior illustrated in Figure 6 is purely a prediction of the model.

At high calcium the the simulated titin elastic chain adopts conformation in both the $p_u(n,s)$ and $p_a(n,s)$ spaces, as illustrated in Figure 7, which shows the state probability as heat maps in the (n,s) space at different time points in the experiment. At time $t = 10^{-3}$ seconds, the binding and unbinding to actin are in an equilibrium balance, with approximately 6% of conformations in bound state. In addition, in the initial state all chains are unfolded with no strain on the titin chain, and thus $p_u(n,s) + p_a(n,s) = \delta(s)\delta_{0,n}$. When chain is rapidly stretched by 0.225 μm, at time $t = 0.1$ seconds, the peak in $p_u(n,s)$ moves to $s \approx 0.18$ μm, predicting that the proximal titin chain is relatively less stretched at this time point in the simulation compared to behavior at low calcium (Figure 5). In addition, in contrast to the calcium-free response, on average only two globular domains per chain are in the unfolded state at $t = 0.2$ seconds, compared to three globular elements unfolded for the simulation at low calcium. Because the proximal chain tends to be less stretched and less unfolded at any given time in the simulation, there is more stress in distal chains, resulting in the Ca^{2+}-dependent increase in peak stress in the simulations.

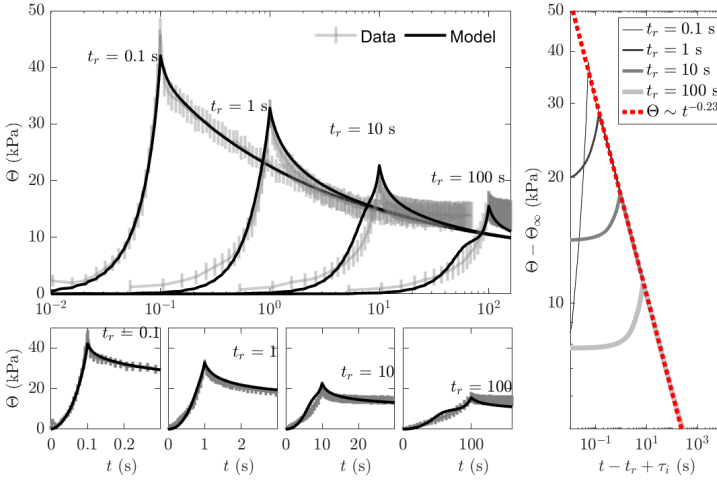Figure 8 shows measured and simulated peak stress as func-

Figure 6: Model fit to stress data following ramp increases in muscle length at high calcium (pCa = 4.51). A. For all time courses the muscle is lengthened from $0.95L_0$ to $1.175L_0$ in linear ramp and then held at the final length to observe the stress decay. The top-left panel show stress data and optimal model fit on a semilog-x plot. The bottom panels shows the peak and initial stress decay on linear scale plots for each ramp time, from $t_r = 0.1$ seconds to $t_r = 100$ seconds. Right: Model-predicted stress decay is shown on a log-log plot.
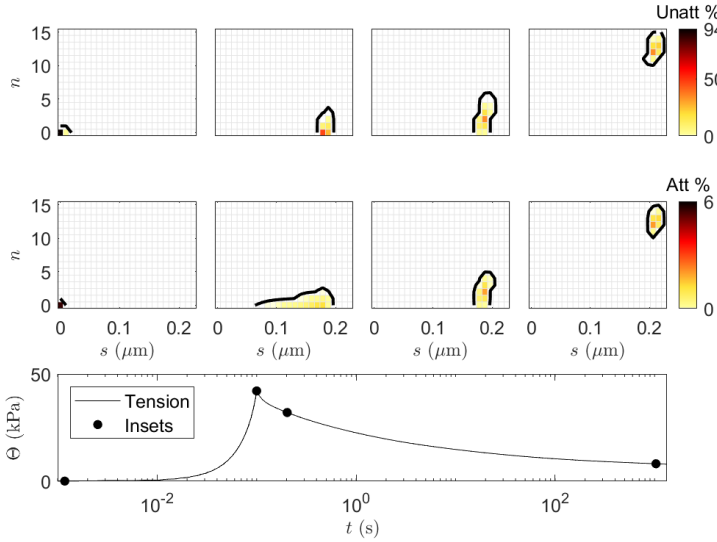

Figure 7: Probability space of simulated chain at high calcium (pCa = 4.51). Top: the probability density $p_u(n, s)$ is illustrated as a heat map, with contours drawn at 1%, at four different times in the simulation of the fast ramp extension experiment. Middle: the probability density $p_a(n, s)$ is illustrated as a heat map, at four different times in the simulation of the fast ramp extension experiment. The bottom panel shows the simulated stress time course and the four time points ($t = 10^{-3}$, 0.1, 0.2, and 1000 seconds) for which the probability densities $p_u(n, s)$ and $p_a(n, s)$ are illustrated in top and middle panels as a per cent of all states.

tions of stretch ramp speed and of calcium concentration, demonstrating that the model effectively captures the trends observed by Baker et al. [1]. The peak stress markedly in-
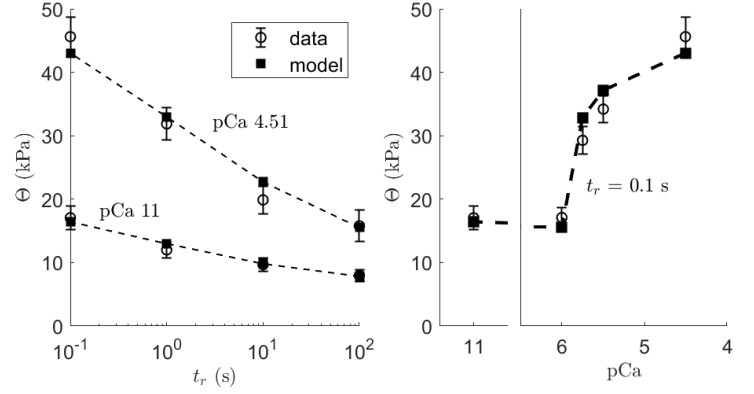

Figure 8: Comparison of measured and simulated peak stress as a function of stretch ramp speed and calcium concentration. Left: peak stress is plotted as a function of ramp speed t_r, comparing measured peaks to model simulations while relaxed (pCa = 11) and at high (pCa = 4.51) calcium concentrations. Right: peak stress at the fastest ramp speed, $t_r = 0.1$ second is plotted as a function of pCa, comparing measured peaks to model simulations.

creases from less than 20 kPa at pCa = 6 to more than 30 kPa at pCa = 5.75, indicating high sensitivity to $[\mathrm{Ca}^{2+}]$ in the micromolar range.

Simulation of preconditioning and cyclic loading

To explore preconditioning behavior we simulated stress response to cyclical sinusoidal loading, with the initial condition of the model in the fully unfolded state: $p_u(n, s) = \delta(s)\delta_{0,n}$. Cyclical loading was simulated by imposing a half sarcomere length of $L(t) = L_0 + (A/2)(\cos(\omega t - \pi) + 1)$, with amplitude $A = L_{max} = 0.225$ μm and frequency $\omega/(2\pi) = 1$ s^{-1}. Predicted stress response to this length time course is illustrated in Figure 9 for the zero-calcium condition. Simulations show that during the initial extension stress increases to a peak of approximately 13 kPa. The peak stress decays with each subsequent cycle of stretch. The right panel of the figure illustrates this hysteresis behavior in a plot of stress versus stretch. Simulations of this stretch protocol for high-calcium conditions (pCa = 4.51) are shown in Figure 10, showing the same general trends as the low-calcium case with higher peak stresses.

The predicted stress-strain behaviors in Figures 9 and 10, showing a drop in peak force from one cycle to the next, are similar to experimental data, for example, from biaxial extension of myocardium [22]. The ability to capture this preconditioning behavior suggests that the model provides a mechanistic basis for understanding and simulating preconditioning phenomena in striated muscle tissue. Unlike experimental results on intact tissue, the simulated hysteresis loops Figures 9 and 10 collapse after several loading cycles. This is because the current model does not account for fluid viscosity in tissue or for refolding of unfolded domains in the chain. Future investigations into titin-mediated preconditioning and hysteresis behavior will require the current model to be extended to
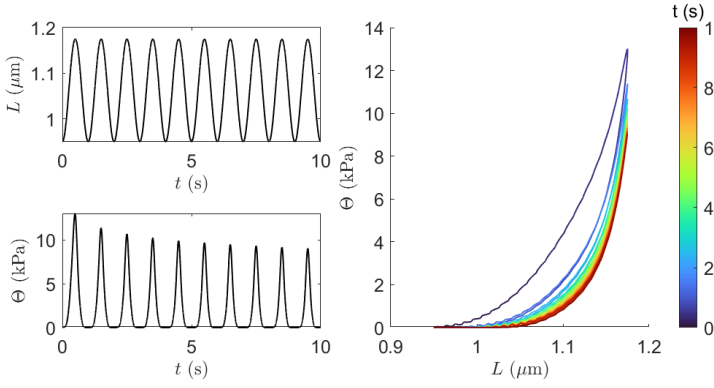
account for refolding events.

Figure 9: Simulation of cyclical loading at zero calcium. The left panel shows the imposed half-sarcomere length $L(t)$ and resulting model-predicted stress $\Theta(t)$ for loading frequency of 1 Hz. The right panel shows the predicted length-stress relationship demonstrating loading-unloading difference and preconditioning of the relaxed muscle.
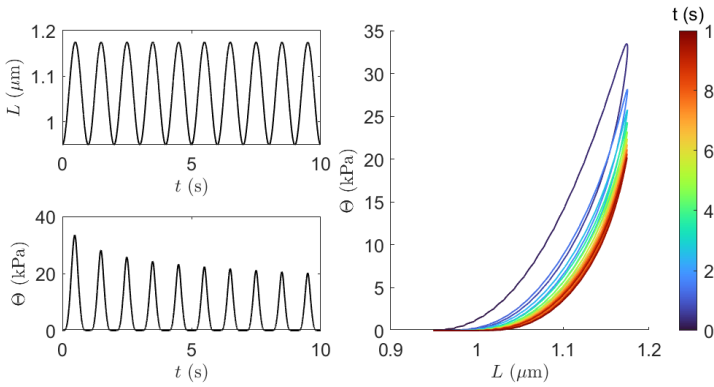

Figure 10: Simulation of cyclical loading at high calcium (pCa = 4.51). The left panel shows the imposed half-sarcomere length $L(t)$ and resulting model-predicted stress $\Theta(t)$ for loading frequency of 1 Hz. The right panel shows the predicted length-stress relationship demonstrating loading-unloading difference and preconditioning of the relaxed muscle.

Discussion

We developed and analyzed a mathematical model of the mechanics of titin in the I band of cardiac muscle, in which titin chains are represented as an ensemble of chains with a probabilistic distribution of strain and degree of unfolding of serial globular Ig elements in the chains. The model is able to capture a broad range of important phenomena that contribute to the nonlinear passive mechanics of myocardial tissue.

In fitting model output to data from Baker et al. [1] the model accurately reflects the observed stress response to a ramp increase in strain, with a concave-up increase in stress during the extension, followed by a decay. As observed by Baker et al. [1], the peak stress achieved in the ramp extension experiment increases with increasing extension speed,

reflecting an apparent viscous component of the stretch response. This phenomenon is predicted to be associated with the dependency of rate of serial titin Ig domain unfolding events on strain. At relatively slower extension rates, Ig domains have more time to unfold during extension, increasing the persistence length of the chain, and resulting in less stress compared to stress at higher extension rates. Regardless of extension speed, when the muscle is held at a fixed length following a ramp extension, the stress decays with a time course that follows $t^{-\beta}$, where β is estimated to be 0.21 from the raw experimental data and 0.23 from model simulations. This power-law decay emerges as a property of the sequence of globular elements in the titin chain. Each element is capable of unfolding and introducing a finite amount of slack into the chain. Equivalently, each unfolding event increases the persistence length of the chain. As each unfolding event introduces slack into the chain the stress sensed by unfolded elements in the sequence decreases, reducing the effective rate of unfolding. Thus, the effective rate of decay decreases as the decay proceeds, resulting in the slow power law decay.

This unfolding of serial globular elements in the titin chain is also predicted to contribute to the hysteresis and preconditioning in the muscle stress-strain relationship. The mechanism underlying hysteresis and preconditioning phenomena in the model follows from the fact that the effective stiffness in the elastic I band region is greatest in the fully folded state. Muscle stretching leads to unfolding, which reduces the effective stiffness of the muscle.

In sum, the unfolding beads-on-a-chain titin model captures the following essential features of passive myocardial mechanics:

1. The dependency of peak stress on rate of muscle extension—the apparent viscous component of the stress response—in a muscle-stretch experiment, as illustrated in Figures 4, 6, and 8.

2. Preconditioning in the passive viscoelastic muscle stress-strain behavior, as illustrated in Figures 9 and 10.

3. The power-law kinetics of stress relaxation, as illustrated in Figures 3 and 4.

Furthermore, by including the calcium-dependent PEVK domain attachment to actin and calcium-dependent chain stiffness, the model captures the observed dependence of peak stress on calcium concentration, as illustrated in Figure 6. This calcium dependence may be important *in vivo* as crossbridge activation and force generation is stimulated by calcium. As shown in the Appendix, the simulated peak stress following the most rapid ramp stretch is particularly sensitive to the PEVK domain attachment mechanism. The predicted stress relaxation kinetics and peak stresses obtained at lower ramp speeds do not depend on including the PEVK attachment mechanism in the simulations.

Model limitations

The model formulation invokes a number of simplifying assumptions, including the simplification that Ig domains unfold only in the titin segment proximal to the PEVK domain. Since PEVK domain attachment to actin does not come into play in low-calcium (pCa = 11) conditions, the assumption that unfolding events occur in only one segment of the chain does not influence the model's behavior at zero or very low $[Ca^{2+}]$. Incorporating distal domain unfolding would make the model more complicated, but may improve the fidelity with which it matches data over a broader range of conditions and protocols.

For applications demonstrated here the model does not account for refolding of Ig domains in the titin chain. However to more accurately simulate hysteresis phenomena, as well as to simulate the contribution of titin mechanics to passive myocardial mechanics *in vivo* it would be necessary to incorporate refolding into the model. Identification of refolding kinetics would require additional experiments.

Although model parameter identification is based on a set of relatively rich and informative data sets, the estimated parameter values likely do not represent a unique global solution. This lack confidence in the global uniqueness of the parameter estimates does not mean that the predictions of the model are flawed, but rather that the parameters are not necessarily well identifiable and their values should be considered valid only in mutual combination and within the context of this model.

Finally, the experiments used to identify the model were conducted at 21° C. In future it would be valuable to attain relevant data at 37° C to investigate how the mechanical phenomena explored here depend on temperature.

1 Acknowledgements

References

[1] A J Baker et al. "Ca^{2+} increases the apparent viscous component of the passive response of cardiac muscle to stretch". In: (2024).

[2] C S Chung et al. "Shortening of the elastic tandem immunoglobulin segment of titin leads to diastolic dysfunction". en. In: *Circulation* 128 (2013), pp. 19–28.

[3] R Emig et al. "Passive myocardial mechanical properties: meaning, measurement, models". en. In: *Biophys Rev.* 13 (2021), pp. 587–610.

[4] D Giganti et al. "Disulfide isomerization reactions in titin immunoglobulin domains enable a mode of protein elasticity". en. In: *Nat. Commun.* 9 (2018), p. 185.

[5] H Granzier and Labeit S. "Cardiac titin: an adjustable multi-functional spring". en. In: *J. Physiol.* 541 (2002), pp. 335–342.

[6] H L Granzier and T C Irving. "Passive tension in cardiac muscle: contribution of collagen, titin, microtubules, and intermediate filaments". en. In: *Biophys. J.* 68 (1995), pp. 1027–1044.

[7] T Heidlauf et al. "A continuum-mechanical skeletal muscle model including actin-titin interaction predicts stable contractions on the descending limb of the force-length relation". en. In: *PLoS Comput. Biol.* 13 (2017), e1005773.

[8] T Heidlauf et al. "A multi-scale continuum model of skeletal muscle mechanics predicting force enhancement based on actin-titin interaction". en. In: *Biomech. Model. Mechanobiol.* 15 (2016), pp. 1423–1437.

[9] M Helmes et al. "Mechanically driven contour-length adjustment in rat cardiac titin's unique N2B sequence: titin is an adjustable spring". en. In: *Circ. Res.* 84 (1999), pp. 1339–1352.

[10] D S Herman et al. "Truncations of titin causing dilated cardiomyopathy". en. In: *N. Eng. J. Med.* 366 (2012), pp. 619–628.

[11] M Herwig et al. "Modulation of Titin-Based Stiffness in Hypertrophic Cardiomyopathy via Protein Kinase D". en. In: *Front Physiol.* 11 (2020), p. 240.

[12] P Hettige et al. "Contributions of Titin and Collagen to Passive Stress in Muscles from mdm Mice with a Small Deletion in Titin's Molecular Spring". en. In: *Int. J. Mol. Sci.* 23 (2022).

[13] M S Kellermayer et al. "Folding-unfolding transitions in single titin molecules characterized with laser tweezers". en. In: *Science* 276 (1997), pp. 1112–1116.

[14] M Kulke et al. "Interaction between PEVK-titin and actin filaments: origin of a viscous force component in cardiac myofibrils". en. In: *Circ. Res.* 89 (2001), pp. 874–881.

[15] E Labeit et al. "Calcium-dependent molecular spring elements in the giant protein titin". en. In: *Proc. Natl. Acad. Sci. U. S. A.* 100 (2003), pp. 13716–13721.

[16] M M LeWinter and H Granzier. "Cardiac titin: a multifunctional giant". en. In: *Circulation* 121 (2010), pp. 2137–2145.

[17] C M Loescher, A J Hobbach, and W A Linke. "Titin (TTN): from molecule to modifications, mechanics, and medical significance". en. In: *Cardiovasc. Res.* 118 (2022), pp. 2903–2918.

[18] J Nedrud et al. "Mechanics on myocardium deficient in the N2B region of titin: the cardiac-unique spring element improves efficiency of the cardiac cycle". en. In: *Biophys. J.* 101 (2011), pp. 1385–1392.

[19] D Nordsletten et al. "A viscoelastic model for human myocardium". In: *Acta Biomaterialia* 135 (2021), pp. 441–457.

[20] Y Peled et al. "Titin mutation in familial restrictive cardiomyopathy". en. In: *Int. J. Cardiol.* 171 (2014), pp. 24–30.

[21] M Rief et al. "Reversible unfolding of individual titin immunoglobulin domains by AFM". en. In: *Science* 276 (1997), pp. 1109–1112.

[22] G Sommer et al. "Quantification of Shear Deformations and Corresponding Stresses in the Biaxially Tested Human Myocardium". en. In: *Ann Biomed Eng.* 43 (2015), pp. 2334–48.

[23] C Squarci et al. "Titin activates myosin filaments in skeletal muscle by switching from an extensible spring to a mechanical rectifier". en. In: *Proc. Natl. Acad. Sci. U. S. A.* 120 (2023), e2219346120.

[24] Y Wu et al. "Changes in titin and collagen underlie diastolic stiffness diversity of cardiac muscle". en. In: *J. Mol. Cell. Cardiol.* 32 (2000), pp. 2151–2162.

Appendix

Data processing

Data from Baker et al. [1] were corrected for drift of the force transducer signal and averaged across multiple experiments. In addition, the data collected under non-zero calcium conditions were corrected to account for incomplete inhibition of active tension development.

Zero drift correction

The experimental protocol to obtain the stress response to ramp stretches included a rapid slack to length $0.8L_0$ between each ramp extension, as illustrated in Figure 2. The force measured during slack was assumed to represent zero force. A cubic spline interpolation between the measured force during the slack periods, and the resulting transient was subtracted from the raw data to correct for drift in the signal.

Data averaging

As a second pre-processing step, the data were averaged by first normalizing all stress data for a given muscle to the highest measured stress Θ_{max} at L_0 in activating solution (maximal $[Ca^{2+}]$) prior to PNB treatment. Next, the data were un-normalized by multiplying by the average Θ_{max}—the average maximum stress across all experiments.

Correction for incomplete inhibition of active tension

Some high-calcium stress time-course data suffer from incomplete PNB inhibition of active tension, resulting in a slow increase in stress following ramp extension. An example data
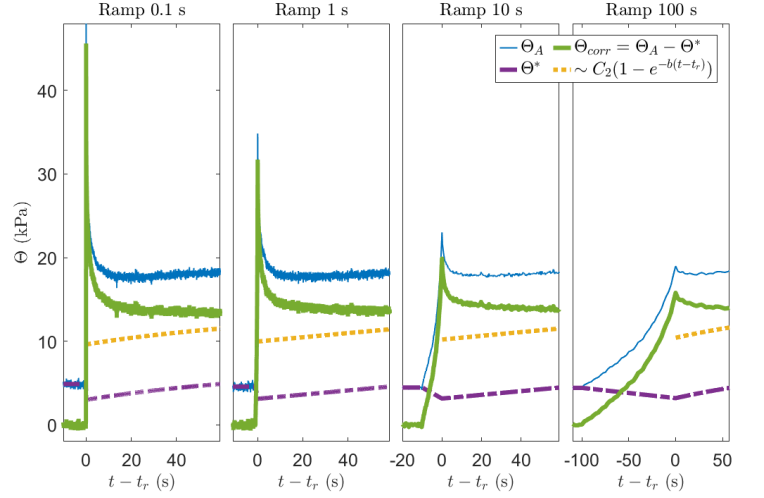

Figure A1: Correction of the remaining crossbridge-force at higher calcium concentrations. Averaged pCa 4.51 data (Θ_A, in blue) are fitted by Θ_F, which consists of two components - power-law term fitting the relaxed decay from previous experiment (not shown) and exponential term approximating remaining active tension (yellow dotted). We shift the exponential component to the steady state stress level to estimate the correction Θ^* (purple) and produce Θ_{corr}.
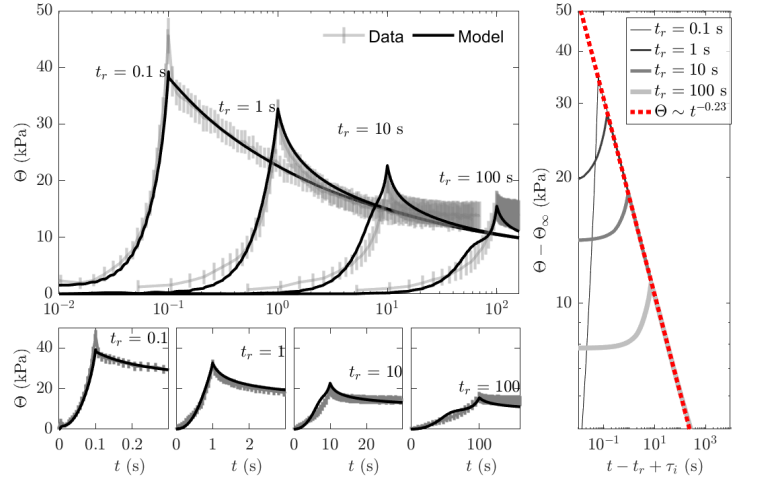

Figure A2: Model simulations of stress response following ramp increases in muscle length at high calcium (pCa = 4.51) with PEVK binding disabled. Simulations are equivalent to simulations shown in Figure 6, but with $k_A = 0$, resulting in no attachment of the titin to actin.

set is illustrated in Figure A1, which shows averaged uncorrected data (Θ_A) as blue. Assuming that the slow increase in stress that occurs following ramp extension is an artefact of incomplete inhibition of active force generation, we fit the raw tail data using a sum of a rising exponential and power-law decay:

$$\Theta_F(t) \approx C_1(t - t_r)^{-\beta} + C_2\left(1 - e^{-b(t-t_r)}\right) + C_3$$

for times greater than 15 seconds after the end of the ramp, and with $\beta = 0.23$, corresponding to the value estimated at

the zero (pCa = 11) calcium.

The exponential part of this fit (Θ^*), shifted to the remaining steady-state force prior to the ramp, is illustrated in purple in Figure A1. Subtracting this exponential component from the raw data, we obtain the corrected data (Θ_{corr}) shown in green.

Effect of PEVK binding

Figure A2 shows simulations of the high-calcium (pCa = 4.51) with PEVK binding disabled. These simulations illustrate that the effect of PEVK binding is apparent only during the peak stress obtained during the fasted ramp.